PHYSICAL REVIEW B **112**, 245424 (2025)

Minimal model of an artificial topological material realized in a two-terminal Josephson junction threaded by Aharonov-Casher fluxes

Luka Medic,[*] Anton Ramšak, and Tomaž Rejec
Jožef Stefan Institute, Jamova 39, SI-1000 Ljubljana, Slovenia
and Faculty of Mathematics and Physics, University of Ljubljana, Jadranska 19, SI-1000 Ljubljana, Slovenia

(Received 13 December 2024; revised 25 February 2025; accepted 7 November 2025; published 23 December 2025)

We investigate a minimal model of a two-terminal Josephson junction with conventional superconducting (SC) leads and a pair of interconnected quantum dots in the presence of two Aharonov-Casher (AC) fluxes. The Andreev bound-state spectrum features Weyl nodes within a three-dimensional synthetic Brillouin zone defined in the space of these AC fluxes and the SC phase difference. The aim is to determine the location and topological charge of these nodes by probing the Berry curvature on closed surfaces that may enclose them. This is achieved by adiabatically varying the superconducting phase difference and AC fluxes along a path on these surfaces and measuring the associated currents. We define the kinematic curvature as the cross product of a tangent vector along the path and the vector of these currents. In the adiabatic regime, the path-averaged kinematic curvature provides a quantized response equal to the topological charge enclosed by the surface, provided the path uniformly and densely covers it.

DOI: 10.1103/mqt7-qzwc

I. INTRODUCTION

Advances in modern physics and technology have spurred great interest in the study of symmetry and topology in condensed matter physics [1–3]. Among these pursuits, significant attention has been drawn to Weyl semimetals (WSMs) [4,5], which host topologically protected Weyl nodes, leading to anomalous phenomena in these materials [6–8].

Treating independent superconducting (SC) phase differences as quasimomenta, an analog of WSMs can be realized in multiterminal Josephson junctions [9,10]. In the subgap regime, the Andreev bound states (ABSs) exhibit Weyl singularities with conical dispersion. Importantly, the authors of Ref. [9] proposed a protocol and a measurable quantity capable of distinguishing between topological and trivial phases in such a system. Following their approach, one applies incommensurate voltages to two SC leads, causing the corresponding SC phase differences to traverse the entire two-dimensional synthetic Brillouin zone (BZ). The remaining independent SC phase differences serve as control parameters, enabling the transition of the system between distinct topological regimes, reflected in the change of transconductance, i.e., a time-averaged response in one SC lead due to voltage applied to another.

Subsequent research has explored systems where a SC control phase difference is replaced by a magnetic flux through the normal region [11–13]. In contrast to Ref. [9], where at least four terminals are needed to realize Weyl topology, these works have shown that a three-terminal junction is sufficient in the presence of the magnetic flux.

In our recent investigation [14], we examined two-terminal Josephson junctions involving the Aharonov-Casher (AC) effect [15–21] in the normal region. The normal region consists of quasi-one-dimensional Rashba quantum wires forming rings, where electrons with opposite spins acquire opposite AC phases [22–25]. (In general, a Rashba spin-orbit interaction induces a non-Abelian AC phase factor [26,27], which, however, reduces to an Abelian one for narrow straight wires [28]). We demonstrated that both the winding and the Chern numbers can be identified in such a junction, and that, since the Weyl nodes are located only at the SC phase difference $\phi = \pi$, the two topological invariants coincide.

In this paper, we analyze a toy model to explicitly demonstrate a topologically nontrivial regime within the class of systems introduced in Ref. [14]. The system's three-dimensional synthetic BZ is in the space of two AC fluxes and the SC phase difference. Unlike SC phase differences, the AC flux in Rashba-gate-controlled rings [28–31] can only be varied over a limited range. Therefore, we consider driving protocols that vary the AC fluxes and the SC phase difference along a path on a small enough closed surface. To determine the enclosed topological charge, we introduce the concept of kinematic curvature, which is defined as the cross product of a tangent vector along the path and the vector of currents associated with AC fluxes and SC phase difference. We demonstrate the connection between the topological charge enclosed by the surface and the path-averaged kinematic curvature. Additionally, we propose a specific driving protocol in which the path is confined to a sphere and use it to compute the path-averaged kinematic curvature for the toy model.

The paper is structured as follows. In Sec. II, we introduce a toy model incorporating two AC fluxes, present a phase diagram identifying gapless regimes that host Weyl nodes, and

---

[*] Contact author: l.medic@windowslive.com

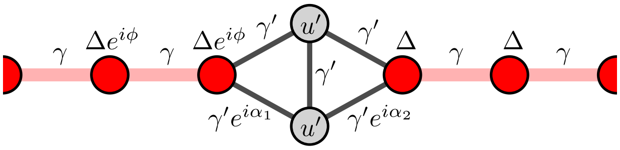

FIG. 1. Superconducting leads (in red) attached to a pair of interconnected quantum dots (gray). The system is threaded by two AC fluxes, inducing phase factors $e^{i\alpha_1}$ and $e^{i\alpha_2}$.

assign a topological charge to each node. In Sec. III, we introduce the kinematic curvature and demonstrate its connection to the topological charge. Finally, in Sec. IV, we provide a concrete example of a driving protocol in which the AC fluxes and SC phase difference evolve along a path covering the sphere.

II. MODEL

Instead of simulating a Josephson junction with gated Rashba quantum wires as proposed in Ref. [14], we employ a simplified toy model (illustrated in Fig. 1) consisting of two SC leads coupled to two interconnected noninteracting quantum dots (QDs), which form two rings threaded by AC fluxes. This toy model effectively captures the key topological aspects of the system discussed in Ref. [14].

The full Bogoliubov–de Gennes Hamiltonian describing the system is provided in the Supplemental Material (SM) S1 [32]. Here, however, we focus on the key components relevant for computing ABSs using the scattering matrix formalism [33]. In Ref. [14], we demonstrated that the topological properties of such systems are identical for both spin sectors. Consequently, we restrict our analysis to the spin sector with spin ↑ (↓) electrons (holes).

The Hamiltonian describing the QDs is

$$H_{\mathrm{QD}} = \begin{bmatrix} u' & -\gamma' \\ -\gamma' & u' \end{bmatrix}, \tag{1}$$

where u' represents the onsite potential on the QDs, and γ' denotes the hopping between them. The hopping between the QDs, along with the tunneling from the SC leads to the QDs, defines two rings, each of which is threaded by an AC flux. As a result, an electron with spin ↑ moving in the anticlockwise direction along a ring acquires an AC phase, either α_1 or α_2, and the tunneling from the SC leads to the QDs can be expressed by the matrix

$$H_T = -\gamma' \begin{bmatrix} 1 & 1 \\ e^{i\alpha_1} & e^{-i\alpha_2} \end{bmatrix}. \tag{2}$$

The minimal model presented includes a single channel per lead, resulting in a 2×2 normal-state scattering matrix S. Neglecting its energy dependence [14,33], it is given by [34]

$$S \equiv \begin{bmatrix} r & t' \\ t & r' \end{bmatrix} = \left(\mathbb{I} - \frac{i}{\gamma} W\right)^{-1} \left(\mathbb{I} + \frac{i}{\gamma} W\right), \tag{3}$$

where r (r') and t (t') denote the reflection and transmission amplitudes for a state incident on the scattering region from the left (right) lead, respectively, γ is the hopping parameter in the leads, and $W = H_T^\dagger H_{\mathrm{QD}}^{-1} H_T$. Closed-form expressions for the reflection and transmission amplitudes are provided in the SM S2 [32].

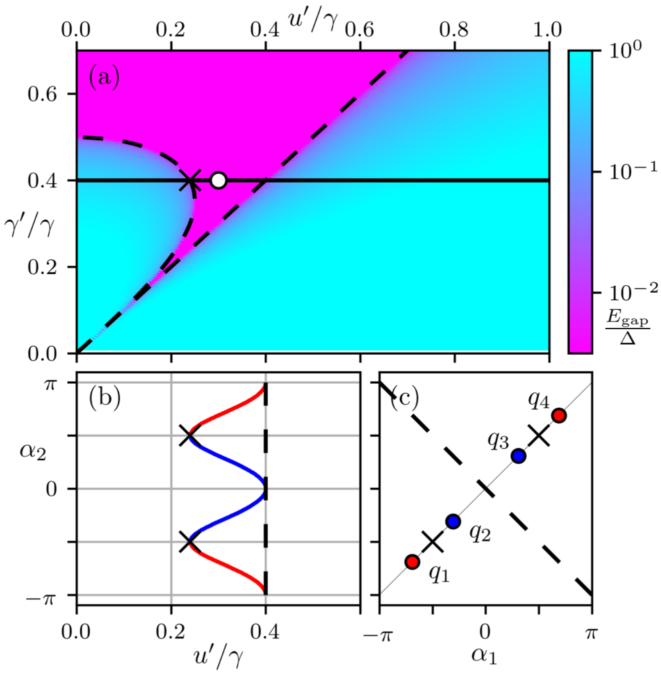

FIG. 2. (a) ABS band gap in the parameter space (u', γ'). The dashed lines delineate the gapped and gapless regimes. (b) Positions of the Weyl nodes with $\gamma'/\gamma = 0.4$ fixed and varying u' [solid line in (a)]. Red (blue) lines represent paths of the Weyl nodes with positive (negative) topological charges. (c) Positions of the Weyl nodes in the synthetic BZ (α_1, α_2) for $u' = 0.3\gamma$ and $\gamma'/\gamma = 0.4$. At $u' = \gamma'$, the ABS energy gap closes along the dashed line.

The energy dispersion of ABSs for a single-channel two-terminal Josephson junction is given by $E_\pm = \pm\Delta\sqrt{1 - T\sin^2(\phi/2)}$, where Δ is the SC gap, ϕ is the SC phase difference, and $T = |t|^2$ is the transmission eigenvalue [33]. Figure 2(a) illustrates the phase diagram in the parameter space of u' and γ', showing the energy gap E_{gap} between the two bands of ABSs in the synthetic BZ. The dashed lines in Fig. 2(a) delineate the gapped regime (in cyan) from the gapless one (purple); for details, see SM S2 [32]. As we increase u' while keeping γ' fixed (e.g., $\gamma' = 0.4\gamma$), two pairs of Weyl nodes with opposite charges emerge at $\alpha_1 = \alpha_2 = \pm\pi/2$ [indicated by crosses in Figs. 2(b) and 2(c)]. Further increasing the parameter u' leads to the separation of the Weyl nodes in the space of AC fluxes, as depicted in Figs. 2(b) and 2(c). At $u' = \gamma'$, the Weyl nodes with negative (positive) charge merge at $\alpha_{1,2} = 0$ (π). Simultaneously, the ABS band gap closes along $\alpha_1 = -\alpha_2$ [dashed line in Fig. 2(c)], resulting in the annihilation of the charges, and the gap forms upon further increasing u'.

Using the values of parameters corresponding to the white dot in Fig. 2(a), Fig. 3 illustrates the phases of reflection and transmission amplitudes. The Weyl nodes are marked as q_i, and their topological charges can be visually inferred from Fig. 3(a): encircling once a single Weyl node in the clockwise direction accumulates a phase of $\pm 2\pi$, corresponding to a topological charge of ± 1. To be more rigorous, following the methodology outlined in Ref. [14], the topological charge $q_W^{(i)}$

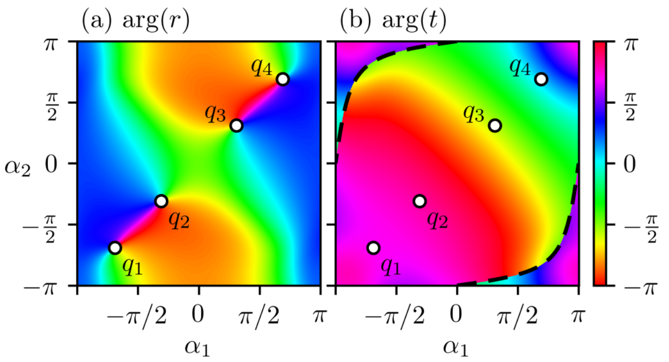

FIG. 3. Phases of (a) the reflection amplitude arg(r) and (b) the transmission amplitude arg(t), plotted as functions of the AC fluxes α_1 and α_2, for $u' = 0.3\gamma$ and $\gamma' = 0.4\gamma$. Positions of Weyl nodes are indicated by q_i. Dashed lines represent a closed SC gap-edge-touching line.

associated with the Weyl point q_i at $\alpha_1 = \alpha_2 = \alpha_W^{(i)}$ and $\phi = \pi$ can be determined from r alone (see SM S2 [32] for a detailed derivation):

$$q_W^{(i)} = \mathrm{sgn}\left[\mathrm{Im}\left(\frac{\partial r}{\partial \alpha_1}\frac{\partial r^*}{\partial \alpha_2}\right)\right]_{\alpha_1=\alpha_2=\alpha_W^{(i)}} = -\mathrm{sgn}\left[\cos\left(\alpha_W^{(i)}\right)\right]. \tag{4}$$

III. KINEMATIC CURVATURE

We propose an observable, termed *kinematic curvature*, and show that it can be used to determine the topological charge q_W. To develop this concept, we first define a vector of currents as $\vec{I} = \langle\psi|\nabla_{\vec{x}}H|\psi\rangle$, where $\vec{x} = [\alpha_1, \alpha_2, \phi]^T$ is a vector containing the AC fluxes and the SC phase difference, and the effective (electron) Hamiltonian acting in the ABS subspace is given by [14]

$$H = \Delta\begin{bmatrix} -(t't'^{\dagger})^{1/2}\cos\frac{\phi}{2} & rt^{\dagger}(tt^{\dagger})^{-1/2}e^{i\phi/2} \\ (tt^{\dagger})^{-1/2}tr^{\dagger}e^{-i\phi/2} & (tt^{\dagger})^{1/2}\cos\frac{\phi}{2}\end{bmatrix}. \tag{5}$$

The first (second) component of $\vec{I}$ is proportional to the spin current in the left (right) ring, while the last component is proportional to the SC current. The wave function $|\psi\rangle$, initially prepared in the ground state, evolves according to the time-dependent Schrödinger equation,

$$i\hbar|\dot{\psi}(\tau)\rangle = H(\tau)|\psi(\tau)\rangle, \tag{6}$$

where τ denotes the time variable.

Assume that $\vec{x}(\tau)$ evolves along a path $\mathcal{P}$ that lies on a closed surface $\mathcal{S}$ within the synthetic BZ, which may potentially contain a Weyl node (or several of them). Let us define the kinematic curvature as

$$\vec{\mathcal{F}} = \frac{\dot{\vec{x}}}{|\dot{\vec{x}}|^2} \times \vec{I}. \tag{7}$$

We will see that this quantity, which arises from the system's transport along a path, is closely related to the Berry curvature. For adiabatic driving, the currents can be expressed up to the first-order correction in velocity $\dot{\vec{x}}$ as [9]

$$\vec{I} = \frac{1}{\hbar}\nabla_{\vec{x}}E_- - \dot{\vec{x}} \times \vec{\mathcal{B}}. \tag{8}$$

The first term represents the adiabatic current, while the second term accounts for the first-order correction, with $\vec{\mathcal{B}} = -\mathrm{Im}(\langle\nabla_{\vec{x}}\psi| \times |\nabla_{\vec{x}}\psi\rangle)$ denoting the Berry curvature. Then, the kinematic curvature can be expressed as

$$\vec{\mathcal{F}} = \vec{\mathcal{B}} + \frac{1}{\hbar}\frac{\dot{\vec{x}}}{|\dot{\vec{x}}|^2} \times \nabla_{\vec{x}}E_- - \frac{\dot{\vec{x}}(\dot{\vec{x}}\cdot\vec{\mathcal{B}})}{|\dot{\vec{x}}|^2}. \tag{9}$$

To eliminate the adiabatic term, one can assume a driving protocol in which the path $\mathcal{P}$ is traversed twice, once in each direction. Let $\hat{n}(\tau)$ denote the unit vector normal to the surface at the point $\vec{x}(\tau)$. Given that $\hat{n}$ and $\dot{\vec{x}}$ are orthogonal, we obtain $\langle\vec{\mathcal{F}}\cdot\hat{n}\rangle_{\mathcal{P}} = \langle\vec{\mathcal{B}}\cdot\hat{n}\rangle_{\mathcal{P}}$, where $\langle\,\rangle_{\mathcal{P}}$ denotes average along the path $\mathcal{P}$, which is traversed in both directions. [The average along $\mathcal{P}$ is defined as $\langle f\rangle_{\mathcal{P}} = \int_{\mathcal{P}} f(s)\mathrm{d}s/\int_{\mathcal{P}}\mathrm{d}s$, where $s = \int_0^{\tau}|\dot{\vec{x}}(\tau')|\mathrm{d}\tau'$ is the arc length.]

Assuming that the path evenly and densely covers the surface $\mathcal{S}$, allowing the line integral to be approximated by a surface integral, we derive that the *path-averaged kinematic curvature*

$$\mathcal{Q} = \frac{|\mathcal{S}|}{2\pi}\langle\vec{\mathcal{F}}\cdot\hat{n}\rangle_{\mathcal{P}} \tag{10}$$

is equal to the topological charge $\sum_i q_W^{(i)}$ enclosed inside $\mathcal{S}$. Here, $|\mathcal{S}|$ denotes the surface area of $\mathcal{S}$. Thus, by measuring the aforementioned currents, one can establish a connection between the system's topology and the (path-averaged) kinematic curvature.

Note that, to ensure adiabatic time evolution, the occupied ABSs must remain sufficiently separated from the unoccupied ones and the continuum states throughout the evolution. This requires that, along the protocol path, both Weyl nodes and SC gap-edge-touching singularities stay adequately distant from $\mathcal{S}$. Specifically, for the model introduced in the previous section, the Weyl nodes and an SC gap-edge-touching line (see SM S2 [32] for details) are indicated in Fig. 3.

IV. DRIVING PROTOCOL EXAMPLE

As a specific example of a driving protocol, we consider the vector $\vec{x}$ confined to the sphere. The goal is to distinguish between spheres that enclose a Weyl point and those that do not.

A point on a sphere of radius R, centered at $\vec{x}_0$, is given by $\vec{x}(\theta,\phi) = \vec{x}_0 + R\,\hat{n}(\theta,\phi)$, where $\theta \in [0,\pi]$ and ϕ are the polar and azimuthal angles, respectively. To evenly traverse the sphere, we set $\phi(\theta) = 2\theta N$, where N is the number of revolutions around the polar axis (see Fig. 4). For the polar angle, we choose $\theta(\tau) = \arccos(1 - \frac{4\tau}{\tau_0})$ for $\tau \in [0, \tau_0/2]$, where τ_0 is the total time to traverse the path in both directions. For $\tau \in [\tau_0/2, \tau_0]$, the path is retraced in the opposite direction. This choice of $\theta(\tau)$ ensures that the speed $|\dot{\vec{x}}|$ remains approximately constant (with an average speed of $\langle|\dot{\vec{x}}|\rangle_{\tau} \approx 8NR/\tau_0$ for large N). Provided that $|\dot{\vec{x}}|$ remains small compared to the energy gap ϵ_{gap} along the path $\mathcal{P}$, the first-order correction in Eq. (8) remains valid throughout the time evolution. The only

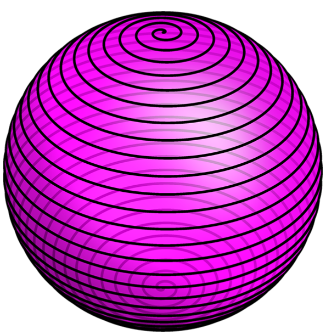

FIG. 4. Depiction of the path on a sphere with $N = 32$ revolutions around the polar axis.

exception occurs near the poles, where $|\dot{\vec{x}}|$ diverges. However, the contribution from this part of the path to the path-averaged kinematic curvature becomes negligible for large N. Moreover, more sophisticated protocols could easily be devised to mitigate this problem.

We numerically verified Eq. (10) by traversing spheres centered at $\vec{x}_0 = [\alpha, \alpha, \pi]^T$, where α specifies the center's position along the diagonal in the plane of AC fluxes (cf. Fig. 3). The quantization of $\mathcal{Q}$ is shown in Fig. 5, which illustrates that paths on spheres enclosing Weyl nodes produce a nonzero quantized response, while those that do not enclose Weyl nodes yield a zero response. The width of the nonzero plateaus is $R\sqrt{2}$. We used the following parameters for the paths: $R = 0.2$, $N = 32$, and $\tau_0 = 2 \times 10^6\, \hbar/\Delta$. Near the edges of the plateaus, we observe spikes whose width decreases as τ_0 increases (see SM S3 [32]). These spikes occur because certain sections of the path come close to a Weyl node, where ϵ_{gap} becomes small compared to $|\dot{\vec{x}}|$, causing the adiabatic approximation in Eq. (8) to break down. The slight asymmetry between the spikes arises from deviations from conical dispersion as one moves away from the Weyl nodes and from the protocol's finite value of N.

In SM S3 [32], an analysis with various values of N and τ_0 is presented, demonstrating the robustness of quantization even for small values of N, such as $N = 8$. The analysis also highlights the breakdown of quantization when the time per revolution around the polar axis, $\frac{\tau_0}{2N}$, approaches the characteristic timescale defined by ϵ_{gap}.

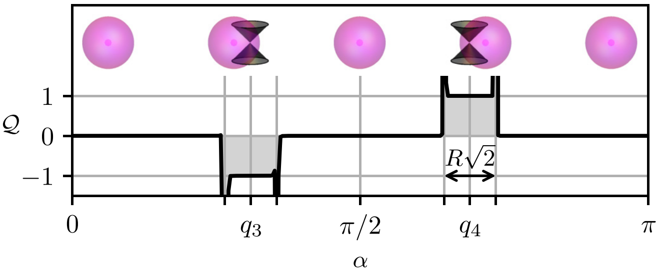

FIG. 5. Quantization of $\mathcal{Q}$. The positions of the Weyl cones, and spheres (with radius R and centers at $\vec{x}_0 = [\alpha, \alpha, \pi]^T$) on which the path $\mathcal{P}$ lies at a given α are shown above the plot.

In the Supplemental Material, we demonstrate that our proposal extends to models with multichannel leads. Furthermore, we present a comprehensive approach, working in the Nambu space to account for both electron and hole degrees of freedom, which yields results nearly identical to those in Fig. 5, with only minor numerical deviations, especially near the spikes at the edges of the quantized plateaus. Finally, the results remain robust even when continuum states are included, which we verified numerically for systems with finite leads. Details of these computations can be found in SM S4–S6 [32].

V. DISCUSSION

In this paper, we presented an approach for experimentally determining the topological properties of a two-terminal Josephson junction with a normal region threaded by AC fluxes. Specifically, we investigated a model in which the normal region consists of two interconnected quantum dots. To measure the topological charges of Weyl nodes emerging in the ABS spectrum, we proposed a protocol involving a path in the space of SC phase difference and AC fluxes that covers a closed surface, potentially enclosing a topological charge. By traversing this path and measuring the superconducting and spin currents, we established a connection between the system's topology and the path-averaged kinematic curvature. Numerical simulations confirmed the effectiveness of the proposed protocol, demonstrating the quantization of $\mathcal{Q}$ with respect to the enclosed topological charge.

We acknowledge experimental challenges associated with tuning the AC fluxes and measuring the spin currents in the rings. In Rashba-gate-controlled semiconductor rings, spin-orbit lengths of the order of 100 nm were reported [19], allowing the variation of the AC flux over several interference periods. Although not directly applicable to our setting, a promising avenue might be germanium hut wires, with electric-field-controlled spin-orbit lengths as low as 2 nm recently observed [21]. Regarding the measurement of spin currents, it has been explored in various theoretical and experimental studies in other contexts [35–39]. Since these works lay a valuable foundation for future developments, we remain optimistic about the experimental validation of our predictions.

For future investigation, it would also be interesting to develop a protocol where the path is confined to the plane $\phi = \pi$ and to identify a measurable quantity directly linked to the winding number in the presence of chiral symmetry [14].

ACKNOWLEDGMENTS

The authors acknowledge support from the Slovenian Research and Innovation Agency (ARIS) under Contract No. P1-0044; A.R. was also supported by Project KTTK21 under Contract No. SN-ZRD/22-27/510 (ARIS).

DATA AVAILABILITY

The data that support the findings of this article are openly available [40].

[1] C.-K. Chiu, J. C. Y. Teo, A. P. Schnyder, and S. Ryu, Classification of topological quantum matter with symmetries, Rev. Mod. Phys. **88**, 035005 (2016).

[2] M. Z. Hasan and C. L. Kane, *Colloquium:* Topological insulators, Rev. Mod. Phys. **82**, 3045 (2010).

[3] X.-L. Qi and S.-C. Zhang, Topological insulators and superconductors, Rev. Mod. Phys. **83**, 1057 (2011).

[4] M. Z. Hasan, S.-Y. Xu, I. Belopolski, and S.-M. Huang, Discovery of Weyl Fermion semimetals and topological Fermi Arc states, Annu. Rev. Condens. Matter Phys. **8**, 289 (2017).

[5] N. P. Armitage, E. J. Mele, and A. Vishwanath, Weyl and Dirac semimetals in three-dimensional solids, Rev. Mod. Phys. **90**, 015001 (2018).

[6] K.-Y. Yang, Y.-M. Lu, and Y. Ran, Quantum Hall effects in a Weyl semimetal: Possible application in pyrochlore iridates, Phys. Rev. B **84**, 075129 (2011).

[7] A. A. Zyuzin and A. A. Burkov, Topological response in Weyl semimetals and the chiral anomaly, Phys. Rev. B **86**, 115133 (2012).

[8] M. N. Chernodub, A. Cortijo, A. G. Grushin, K. Landsteiner, and M. A. H. Vozmediano, Condensed matter realization of the axial magnetic effect, Phys. Rev. B **89**, 081407(R) (2014).

[9] R.-P. Riwar, M. Houzet, J. S. Meyer, and Y. V. Nazarov, Multi-terminal Josephson junctions as topological matter, Nat. Commun. **7**, 11167 (2016).

[10] E. Eriksson, R.-P. Riwar, M. Houzet, J. S. Meyer, and Y. V. Nazarov, Topological transconductance quantization in a four-terminal Josephson junction, Phys. Rev. B **95**, 075417 (2017).

[11] J. S. Meyer and M. Houzet, Nontrivial Chern numbers in three-terminal Josephson junctions, Phys. Rev. Lett. **119**, 136807 (2017).

[12] H.-Y. Xie, M. G. Vavilov, and A. Levchenko, Topological andreev bands in three-terminal Josephson junctions, Phys. Rev. B **96**, 161406(R) (2017).

[13] L. Peralta Gavensky, G. Usaj, and C. A. Balseiro, Topological phase diagram of a three-terminal Josephson junction: From the conventional to the Majorana regime, Phys. Rev. B **100**, 014514 (2019).

[14] L. Medic, A. Ramšak, and T. Rejec, Artificial topological insulator realized in a two-terminal Josephson junction with Rashba spin-orbit interaction, Phys. Rev. Res. **7**, 013166 (2025).

[15] Y. Aharonov and A. Casher, Topological quantum effects for neutral particles, Phys. Rev. Lett. **53**, 319 (1984).

[16] A. Cimmino, G. I. Opat, A. G. Klein, H. Kaiser, S. A. Werner, M. Arif, and R. Clothier, Observation of the topological Aharonov-Casher phase shift by neutron interferometry, Phys. Rev. Lett. **63**, 380 (1989).

[17] H. Mathur and A. D. Stone, Quantum transport and the electronic Aharonov-Casher effect, Phys. Rev. Lett. **68**, 2964 (1992).

[18] M. König, A. Tschetschetkin, E. M. Hankiewicz, J. Sinova, V. Hock, V. Daumer, M. Schäfer, C. R. Becker, H. Buhmann, and L. W. Molenkamp, Direct observation of the Aharonov-Casher phase, Phys. Rev. Lett. **96**, 076804 (2006).

[19] T. Bergsten, T. Kobayashi, Y. Sekine, and J. Nitta, Experimental demonstration of the time reversal Aharonov-Casher effect, Phys. Rev. Lett. **97**, 196803 (2006).

[20] X. Liu, M. F. Borunda, X.-J. Liu, and J. Sinova, Control of Josephson current by Aharonov-Casher phase in a Rashba ring, Phys. Rev. B **80**, 174524 (2009).

[21] H. Liu, T. Zhang, K. Wang, F. Gao, G. Xu, X. Zhang, S.-X. Li, G. Cao, T. Wang, J. Zhang, X. Hu, H.-O. Li, and G.-P. Guo, Gate-Tunable spin-orbit coupling in a Germanium hole double quantum dot, Phys. Rev. Appl. **17**, 044052 (2022).

[22] Y. A. Bychkov and E. I. Rashba, Oscillatory effects and the magnetic susceptibility of carriers in inversion layers, J. Phys. C **17**, 6039 (1984).

[23] A. Manchon, H. C. Koo, J. Nitta, S. M. Frolov, and R. A. Duine, New perspectives for Rashba spin–orbit coupling, Nat. Mater. **14**, 871 (2015).

[24] D. Tomaszewski, P. Busz, R. López, R. Žitko, M. Lee, and J. Martinek, Aharonov-Bohm and Aharonov-Casher effects for local and nonlocal Cooper pairs, Phys. Rev. B **97**, 214506 (2018).

[25] D. Tomaszewski, P. Busz, R. López, R. Žitko, M. Lee, and J. Martinek, Aharonov-Bohm and Aharonov-Casher effects in a double quantum dot Josephson junction, Phys. Rev. B **98**, 174504 (2018).

[26] Y. Avishai, K. Totsuka, and N. Nagaosa, Non-Abelian Aharonov–Casher phase factor in mesoscopic systems, J. Phys. Soc. Jpn. **88**, 084705 (2019).

[27] S. Oh and C.-M. Ryu, Persistent spin currents induced by the Aharonov-Casher effect in mesoscopic rings, Phys. Rev. B **51**, 13441 (1995).

[28] M. Governale, F. Taddei, and R. Fazio, Pumping spin with electrical fields, Phys. Rev. B **68**, 155324 (2003).

[29] R. Citro and F. Romeo, Pumping in a mesoscopic ring with Aharonov-Casher effect, Phys. Rev. B **73**, 233304 (2006).

[30] B. H. Wu and J. C. Cao, Analysis of spin pumping in asymmetric ring conductors with the Aharonov-Casher effect, Phys. Rev. B **75**, 113303 (2007).

[31] D. Grundler, Large Rashba splitting in inas quantum wells due to electron wave function penetration into the Barrier layers, Phys. Rev. Lett. **84**, 6074 (2000).

[32] See Supplemental Material at http://link.aps.org/supplemental/10.1103/mqt7-qzwc for the full Bogoliubov–de Gennes Hamiltonian, an analytical examination of the model, an analysis of the protocol parameters, an extension to multichannel leads, a formulation of time evolution in the Nambu space, and the exact time evolution of the BdG Hamiltonian, which includes Refs. [41,42].

[33] C. W. J. Beenakker, Universal limit of critical-current fluctuations in mesoscopic Josephson junctions, Phys. Rev. Lett. **67**, 3836 (1991).

[34] F.-M. Dittes, The decay of quantum systems with a small number of open channels, Phys. Rep. **339**, 215 (2000).

[35] F. Meier and D. Loss, Magnetization transport and quantized spin conductance, Phys. Rev. Lett. **90**, 167204 (2003).

[36] F. Schütz, M. Kollar, and P. Kopietz, Persistent spin currents in mesoscopic Heisenberg rings, Phys. Rev. Lett. **91**, 017205 (2003).

[37] Q.-f. Sun, X. C. Xie, and J. Wang, Persistent spin current in nanodevices and definition of the spin current, Phys. Rev. B **77**, 035327 (2008).

[38] S. O. Valenzuela and M. Tinkham, Direct electronic measurement of the spin Hall effect, Nature (London) **442**, 176 (2006).

[39] F. Nichele, S. Hennel, P. Pietsch, W. Wegscheider, P. Stano, P. Jacquod, T. Ihn, and K. Ensslin, Generation and detection of spin currents in semiconductor nanostructures with strong spin-orbit interaction, Phys. Rev. Lett. **114**, 206601 (2015).

[40] L. Medic, A. Ramšak, and T. Rejec, A minimal model of an artificial topological material realized in a two-terminal Josephson junction threaded by Aharonov-Casher fluxes [Dataset], Zenodo (2025), doi:10.5281/zenodo.15658058.

[41] T. Martin and R. Landauer, Wave-packet approach to noise in multichannel mesoscopic systems, Phys. Rev. B **45**, 1742 (1992).

[42] C. W. J. Beenakker, Random-matrix theory of quantum transport, Rev. Mod. Phys. **69**, 731 (1997).